Journal of Materials Chemistry B

PAPER

View Article Online
View Journal | View Issue

Cite this: J. Mater. Chem. B, 2018, 6, 7420

NIR organic dyes based on phenazine-cyanine for photoacoustic imaging-guided photothermal therapy†

Yongchao Yan,[a] Jiawen Chen,[b] Zhijuan Yang,[b] Xiao Zhang,[a] Zhuang Liu *[b] and Jianli Hua *[a]

Received 4th July 2018,
Accepted 4th October 2018

DOI: 10.1039/c8tb01750f

rsc.li/materials-b

As non-invasive diagnosis and therapy methods, photoacoustic (PA) imaging and photothermal therapy (PTT) have attracted extensive attention. Herein, two new acceptor–donor–acceptor near-infrared organic phenazine-cyanine dyes **PH-1** and **PH-2** were reported for photoacoustic imaging-guided photodynamic therapy. In the strong donor phenazine molecule, the electron-withdrawing indole salt unit was introduced for absorption to the near-infrared region. To improve water solubility, the two organic dyes were assembled with human serum albumin (HSA) to form nanoparticles of appropriate sizes, *i.e.*, **PH-1@HSA** and **PH-2@HSA**, which showed excellent stability in both weakly acidic and weakly basic environments. Moreover, the results showed that **PH-1@HSA** and **PH-2@HSA** nanoparticles can effectively transform luminous energy to thermal energy *in vitro* and *in vivo*, and they can be utilized for PA imaging. Importantly, **PH-1@HSA** can accumulate in mice subcutaneous tumors by enhanced permeability and retention (EPR) and damage cancer tissues effectively.

Introduction

Nowadays, cancer has become one of the major threats to human health; thus, it is urgent to develop effective methods for diagnosis and therapy.[1] Chemotherapy is the dominant measure to treat cancer; nevertheless, most of the conventional chemotherapeutic drugs as single agents have not satisfied clinical requirements because of multidrug resistance (MDR) and toxic side effects.[2] In addition, due to other common methods, such as radiotherapy and surgery, cancer patients usually suffer pain during the treatment. Recently, noninvasive and mild methods for diagnosis and therapy such as photoacoustic (PA) imaging and photothermal therapy (PTT) have attracted wide attention due to minimal harm to normal tissues and effective tumor lethality.[3–5] PA imaging is a non-invasive technique that gathers photo-induced ultrasound signals from a pulsed laser irradiating tissue, combining high-contrast and spectroscopic-based specificity of optical imaging with high spatial resolution of ultrasound imaging.[6] Compared with traditional optical imaging, PA imaging provides deeper tissue penetration and higher spatial resolution *in vivo* because ultrasound scatters to a much lesser extent relative to light while passing through tissues.

PTT kills cancer cells by employing agents that convert luminous energy to thermal energy,[7] and it also has some merits including non-invasiveness, low side effects, high selectivity and no resistance.[8–10] The current NIR agent materials include gold-nanomaterials,[11,12] carbon nanomaterials,[13] transition-metal dichalcogenides,[14] organic polymers[15,16] and NIR dyes.[17] Compared to inorganic materials, organic PTT agents show some superiorities such as regulable absorption spectrum, biodegradability and rapid elimination in biological tissues.[18,19] Due to these reasons, it is essential to design and synthesize NIR organic dyes for PA imaging and PTT.

In previous studies, PTT agents based on NIR dyes were almost cyanine,[20] BODIPY,[21,22] diketopyrrolopyrrole (DPP)[23,24] and benzobisthiadiazole[25,26] derivatives. These dyes usually exhibit a donor–acceptor–donor (D–A–D) structure, in which BODIPY, DPP and benzobisthiadiazole are electron-withdrawing groups attached to different electron donors. Stronger donor group and acceptor group can decrease the energy gap between HOMO and LUMO, which causes a red shift.[27,28] However, reports on A–D–A structured NIR dyes for photoacoustic imaging-guided photodynamic therapy are few. Reduced phenazine, which possesses many modification sites, strong electron-donating

[a] Key Laboratory for Advanced Materials and School of Chemistry and Molecular Engineering, East China University of Science and Technology, 130 Meilong Road, Shanghai 200237, China. E-mail: jlhua@ecust.edu.cn
[b] Institute of Functional Nano & Soft Materials (FUNSOM), Jiangsu Key Laboratory for Carbon-Based Functional Materials & Devices, Soochow University, Suzhou 215123, China. E-mail: zliu@suda.edu.cn

† Electronic supplementary information (ESI) available: Characterization data for all compounds, additional spectroscopic data, MS titrations. See DOI: 10.1039/c8tb01750f

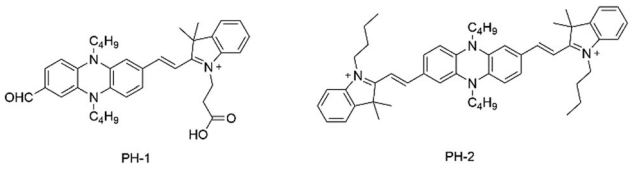

Scheme 1 Structures of **PH-1** and **PH-2**.

ability and excellent stability, has been used to design fluorescent probes.[29–31] When nitrogen atoms were linked with *n*-butyl groups, the phenazine group changed to an electron-rich donor group from initial electron-deficient group. Meanwhile, indole salt derivatives are common electron-withdrawing groups because of the presence of positive charges. In this study, a butyl phenazine donor and alkyl indole salt acceptor were employed to design and synthesize NIR phenazine-cyanine dyes **PH-1** and **PH-2** for PA imaging and PTT, in which intramolecular charge transfer (ICT) occurred from alkyl phenazine to the alkyl indole salt. Unlike the acceptor–donor–acceptor (A–D–A) structure of **PH-2** with two alkyl indole salt groups on both sides of phenazine, the retained carbaldehyde moiety on **PH-1** resulted in an acceptor–donor–another acceptor (A–D–A′) structure with two different routes of the ICT process. We hope to adjust the absorption spectrum by changing the electron-withdrawing group. We have described the synthesis as well as the optical properties of two phenazine-cyanine dyes **PH-1** and **PH-2** (Scheme 1), characteristics of **PH-1@HSA** and **PH-2@HSA** and the preliminary investigations of PA images and PTT in nude mouse based on **PH-1@HSA**.

Results and discussion

Synthesis of PH-1 and PH-2

The synthetic route for phenazine-cyanine dyes is shown in Fig. 1. Phenazine was first reduced by sodium hydrosulfite. Then, hydrogen linked to nitrogen atoms was substituted by *n*-butyl group in an alkaline environment to obtain compound **2**.

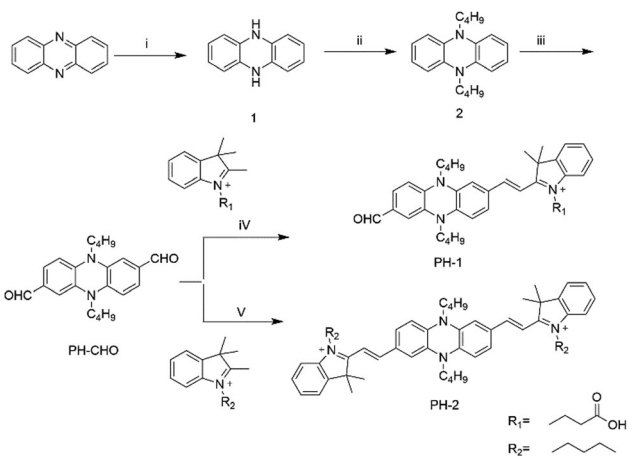

Fig. 1 Synthetic routes of **PH-CHO**, **PH-1** and **PH-2**. Reagents and conditions: (i) $Na_2S_2O_4$, EtOH, H_2O, 80 °C. (ii) NaOH, tetrabutylammonium bromide, iodobutane, DMSO, H_2O, 40 °C (iii) $POCl_3$, 0 °C, DMF, 60 °C. (iV) Piperidine, MeCN, 80 °C. (V) CH_3COONH_4, CH_3COOH, 70 °C.

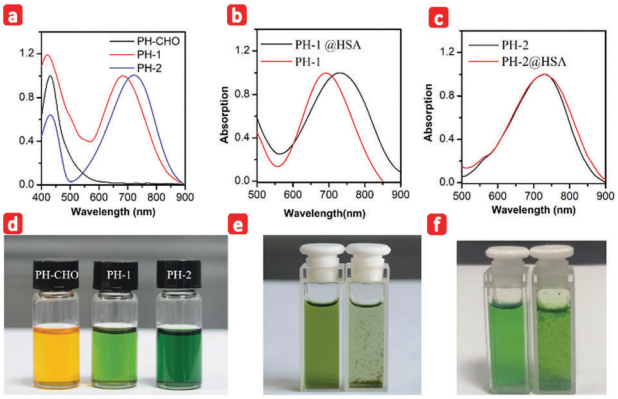

Fig. 2 (a) UV-visible absorption spectra of **PH-CHO**, **PH-1** and **PH-2** in DMSO : PBS solution (v : v = 3 : 7) at 10 μM. (b) Absorption normalization of **PH-1** and **PH-1@HSA**. (c) Absorption normalization of **PH-2** and **PH-2@HSA**. (d) Photograph of **PH-CHO**, **PH-1** and **PH-2** in solution. (e) Photograph of **PH-1** (right) and **PH-1@HSA** (left) in PBS. (f) Photograph of **PH-2** (right) and **PH-2@HSA** (left) in PBS.

The important intermediate **PH-CHO** was obtained by Vilsmeier–Haack reaction. The asymmetric cyanine dye **PH-1** was obtained through the reaction of *n*-butyric acid indole iodide salt with the corresponding phenazine aldehyde in piperidine at 80 °C. The symmetric cyanine dye **PH-2** was synthesized by Knoevenagel reaction of **PH-CHO** and butyl indole iodide salt in acetic acid at 70 °C. These main compounds were characterized by ^{1}H NMR, ^{13}C NMR and MS. The details of the structural identification spectra are given in the ESI.†

Optical properties of PH-CHO, PH-1 and PH-2

As shown in Fig. 2a, the maximum absorption wavelength of **PH-CHO** was 430 nm ($\varepsilon = 1.65 \times 10^4$ M^{-1} cm^{-1}). When an aldehyde group was replaced by alkyl indole salt, the maximum absorption wavelength of **PH-1** was about 690 nm ($\varepsilon = 1.25 \times 10^4$ M^{-1} cm^{-1}). Compared to the observation for **PH-CHO**, the maximum absorption of **PH-1** red-shifted by 255 nm due to the ICT process from alkyl phenazine to the alkyl indole salt. When another alkyl indole salt was introduced, the maximum absorption of **PH-2** further increased to 720 nm (Fig. 2a, blue line, $\varepsilon = 4.25 \times 10^4$ cm^2 mol^{-1}), which showed about 30 nm red-shift compared to that of **PH-1**. Significant differences among three dyes could be observed (shown in Fig. 2d) by the naked eye, in which the solution changed from orange-yellow, green to deep green. Furthermore, **PH-1** and **PH-2** showed much better photostabilities compared with ICG (Fig. S1, ESI†). When exposed to white light for 50 min, **PH-1** almost stayed the same, whereas ICG showed a decrease to ~10%. The absorption spectra of both **PH-1** and **PH-2** were more than 800 nm, suggesting that they have potential applications in PA imaging and PTT.

Characteristics of PH-1@HSA and PH-2@HSA

Poor water solubility limits the biological applications of NIR dyes.[32] Recently, human serum albumin (HSA), a principal protein in plasma, was employed as a drug carrier due to its improved water solubility, reduced immunogenicity, low levels

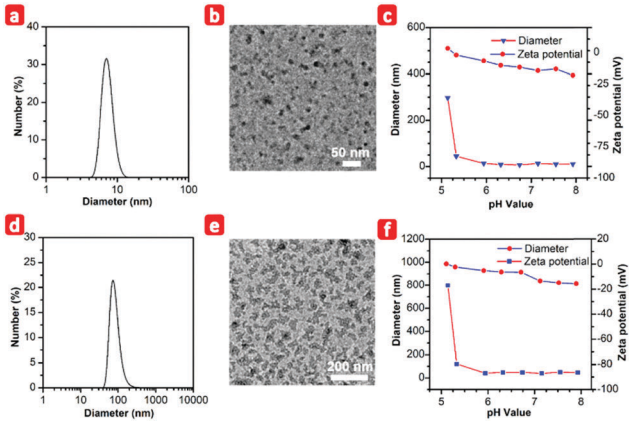

Fig. 3 (a) DLS examination for size of **PH-1@HSA** in PBS buffer, pH = 7.4. (b) TEM image of **PH-1@HSA** NPs. (c) Average diameter and zeta potential of **PH-1@HSA** in different pH value B–R buffers. (d) DLS examination for size of **PH-2@HSA** in PBS buffer, pH = 7.4. (e) TEM image of **PH-2@HSA** NPs. (f) Average diameter and zeta potential of **PH-2@HSA** in different pH value B–R buffers.

of mononuclear phagocyte system clearance, prolonged circulatory half-life, improved pharmacokinetic properties, and versatile roles.[33–35] To improve biocompatibility of **PH-1** and **PH-2**, they were self-assembled with HSA to form nanoparticles named as **PH-1@HSA** and **PH-2@HSA**. As shown in Fig. 2e and f, clear floccules could be seen when **PH-1** was directly added to PBS solution, which is due to the poor water solubility. Organic dye nanoparticles showed excellent solubility in pure water. The same phenomenon could also be observed for **PH-2**. Subsequently, the absorption spectra (Fig. 2b and c) of **PH-1** and **PH-2** before and after assembly were measured. The peak of **PH-1@HSA** NPs showed 40 nm red-shift compared to that of **PH-1**, which was caused by molecular aggregation. **PH-2@HSA** showed no clear red-shift, which may be because of the improved water solubility of two alkyl indole salts. Besides, the spectrum of NPs was wider than those of **PH-1** and **PH-2**, which was ascribed to intermolecular interactions. The bathochromic-shift and broadening of the spectrum implied that **PH-1** species were indeed self-assembled with HSA to form nanoparticles. Then, the morphology and particle size of two nanoparticles were studied by transmission electron microscopy (TEM) and dynamic light scattering (DLS). As shown in the TEM image (Fig. 3b), **PH-1@HSA** exhibited spherical morphology and there was no distinct aggregation. Furthermore, DLS showed that the average diameter of **PH-1@HSA** was about 10 nm, which was the appropriate size for enrichment in tumor. The shape of **PH-2@HSA** NPs was irregular and the average diameter was about 50 nm.

Stability of NPs in different pH environments

The micro-environment of tumors is weakly acidic, whereas that of normal tissues is weakly basic;[36] the nanoparticles should be stable in both weakly acidic and weakly basic environments. Thus, the pH stabilities of two nanoparticles were evaluated by DLS. NPs were attenuated with different pH values of Britton–Robinson (B–R) buffer and then, the average sizes and zeta potentials were measured. As shown in Fig. 3c and f, two nanoparticles showed appropriate stability in both weakly acidic and weakly basic environments. Form pH 5.5 to 8.0, the sizes of **PH-1@HSA** NPs and **PH-2@HSA** NPs showed almost no variation, which manifested that nanoparticles could be stable with negligible aggregation in both normal tissues and tumors. However, when the pH value was less than 5.5, the size of NPs increased abruptly. Meanwhile, the zeta potential changed to a positive value from negative value, which was a possible reason for NP aggregation. In the weakly basic micro-environment, the zeta potentials of two NPs were negative, which resulted in stability in the serum.

Photothermal *in vitro*

To investigate the therapeutic effect, different concentrations of **PH-1@HSA** (0, 5, 10, 20, 40 and 80 μM) in solutions were tested. As shown in Fig. 4a and d, the elevated temperature was related to the nanoparticles' concentration and exposure duration. The temperature of NP solution increased rapidly within 3 minutes and then rose progressively and remained steady. The temperature difference of pure PBS buffer was only about 5 °C when exposed to laser, whereas that of 80 μM **PH-1@HSA** rose to about 36.7 °C. This suggested that NPs can absorb light and transfer luminous energy to thermal energy, which causes temperature increase. The temperature of **PH-1@HSA** NP (20 μM) PBS buffer reached 49.3 °C within 300 s, which is high enough to kill cancer cells. At the same condition, the temperature of **PH-2@HSA** (20 μM) NP PBS buffer reached 52.5 °C. However, when the concentration of **PH-2@HSA** was higher than 40 μM, the temperature curve rose and then descended.

Then, the photothermal stabilities of **PH-1@HSA** and **PH-2@HSA** were further evaluated by monitoring the variation in the temperature of the solution (20 μM) during irradiation with 808 nm laser for 3 min, followed by natural cooling for 3 min

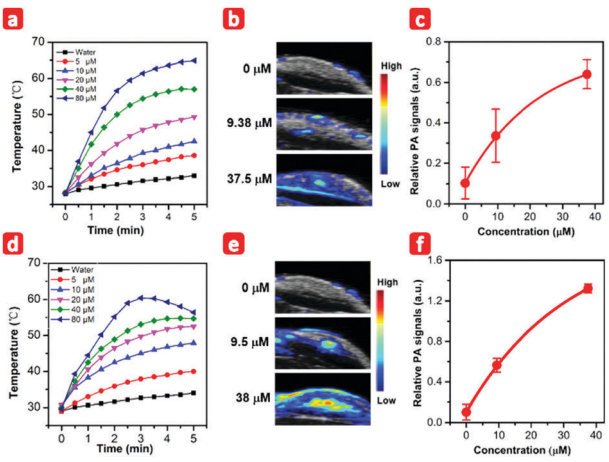

Fig. 4 Temperature curves of different concentrations of **PH-1@HSA** (a) and **PH-2@HSA** (d) in PBS buffer under 808 nm laser, 1.0 W cm^{-2}; PA images of subcutaneous tissue with different concentrations of **PH-1@HSA** (b) and **PH-2@HSA** (e). Relation between intensity of relative PA signals and concentrations of **PH-1@HSA** (c) and **PH-2@HSA** (f).

after the laser was turned off for five cycles. As shown in Fig. S2 (ESI†), the temperature rose when **PH-1@HSA** were exposed to laser and then declined when the laser was turned off. In the next several cycles, the temperature maximum almost remained unchanged. However, the temperature maximum of **PH-2@HSA** decreased gradually (Fig. S3, ESI†). In the first cycle, the highest temperature was about 52 °C; nevertheless, the highest temperature in the fifth cycle was just round 42 °C. Furthermore, the color of **PH-2@HSA** changed from deep green to yellow green. This demonstrated that **PH-1** performed better than **PH-2** with respect to photothermal stability. Based on the above reasons, **PH-1** was chosen for further tests.

PA *in vivo*

Considering that PTT agents are mostly applied for PA imaging, the performances of **PH-1@HSA** and **PH-2@HSA** were verified using nude mouse (Fig. 4b and e). NPs diluted with PBS buffer were injected into back subcutaneous tissues of mice, which were irradiated by 808 nm pulse laser, and the PA signal was collected by an ultrasonic detector. As shown in Fig. 4b and e, NPs exhibited a clear PA signal in mice back subcutaneous tissues, which showed a conspicuous contrast to that of background. The enhanced intensity of PA signal was associated with the increase in NP concentration. When pure PBS buffer was injected in mice back, a small ultrasonic signal could also be detected, which may be due to hemoglobin. As the NP concentration was about 38 μM, the PA intensity of **PH-1@HSA** showed 6.2-fold enhancement to PBS, whereas that of **PH-2@HSA** showed 12.8-fold enhancement. The result was in accordance with photo-thermal data, which suggested that PA conversion efficiency is associated with photothermal conversion efficiency. Considering the enhanced PA signals related to NP concentration, **PH-1** and **PH-2** have potential applications in PA imaging.

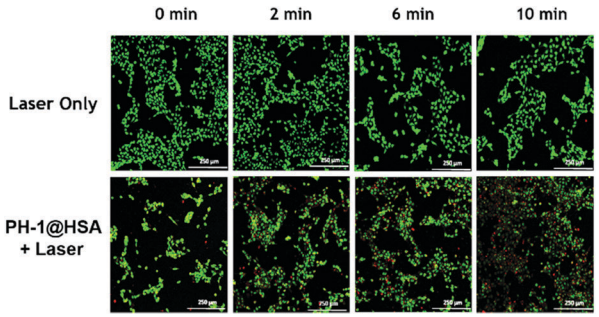

Fig. 5 Fluorescence confocal image of 4T1 cells treated by laser irradiation only; incubation with **PH-1@HSA** and laser irradiation for different times (808 nm laser: 0.8 W cm^{-2}, concentration = 20 μM, scale bar = 250 μm).

Phototoxicity to 4T1 cells

Subsequently, the cytotoxicity of NPs to 4T1 cells was assessed by MTT. The cell viability was measured by an MTT assay using a microplate absorbance reader (Model 680, Bio-Rad) at 570 nm. In the dark state for 48 h, when the concentration was lower than 25 μM, the cell viability was more than 50% (Fig. S4, ESI†), which suggested NPs show suitable toxicity in the dark state. In the experimental group, 4T1 cells were exposed to 808 nm laser (0.8 W cm^{-2}) for 20 min in the presence of **PH-1@HSA**, and conspicuous photo-toxicity could be confirmed. When the concentration was increased from 1.25 to 20 μM, the cell viability declined rapidly, and the decrease was related to the increase in NPs (as shown in Fig. S5, ESI†). When the concentration was 20 μM, about half of the cells were killed, which suggested that **PH-1@HSA** possessed adequate cytotoxicity in the presence of a laser.

To confirm the PTT effect *in vitro*, photo-toxicity was also evaluated by confocal CLSM (confocal laser scanning microscopy) imaging. The Calcine AM (green) and propidium iodide (red) were utilized to distinguish live and dead cells. Also, 4T1 cells were divided into two groups: control group (laser only) and experimental group (**PH-1@HSA** + laser). As shown in Fig. 5, in the control group, a small red region could be observed, which suggested that almost all of the cells had survived. In the experimental group, the red region enlarged along with irradiating time. When the cells were incubated with NPs and exposed to laser for 0 min, the phenomenon was similar with that of the control group, which also indicated the low toxicity in dark condition. After exposure for 2, 6 and 10 min, the red region became more clear, implying that more 4T1 cells were killed. CLSM imaging confirmed that **PH-1@HSA** with measurable concentration indeed damaged cells only in the presence of a laser.

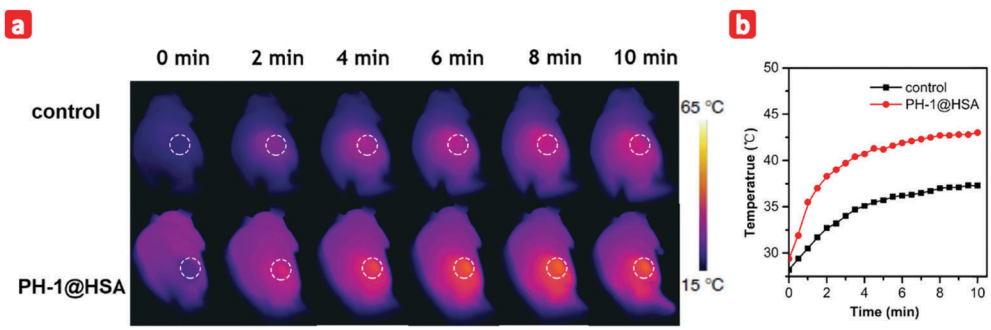

Fig. 6 (a) Thermal image of nude mouse in control group and experimental group at different illuminating times. (b) Relational group of tumor temperature of mice in control group and experimental group and time. Tumor models were built with 4T1 cells, and **PH-1@HSA** (200 μL, 500 μM) were injected in the tail of mice.

Photothermal *in vivo*

To identify **PH-1@HSA** photo-thermal effect *in vivo*, mice experiments were performed. NPs were injected in nude mouse tail; after 4 hours, tumors[37] were irradiated by an 808 nm laser (0.8 W cm^{-2}). As shown in Fig. 5, in the control group, the temperature of tumors was ~37 °C when exposed to laser for 10 min. In the experimental group, the temperature gradually rose with time and reached ~43 °C after 10 min, which can damage cancer tissues effectively.[38] As shown in Fig. S6 (ESI†), tumor tissue necrosis could be observed after PTT, and the size of tumor reduced conspicuously 5 days later. In the control group, tumors enlarged gradually. Photo-thermal imaging implied that NPs can indeed accumulate in tumors within 4 h by the EPR effect and generate heat *in vivo*. Thus, **PH-1@HSA** can be utilized for PTT (Fig. 6).

Conclusions

In summary, two new A–D–A NIR organic phenazine-cyanine dyes **PH-1** and **PH-2** were developed for PA imaging and PTT. The absorption wavelengths of compounds broadened to the near-infrared region *via* introducing stronger electron-withdrawing groups into butylphenazine for structuring strong ICT. The water solubility of dyes improved by self-assembly with HSA, and NPs existed steadily in both weakly acidic and weakly basic environments, which indicated that NPs can work in blood circulation. Furthermore, **PH-1@HSA** and **PH-2@HSA** could transfer luminous energy to thermal energy effectively *in vitro*. Importantly, **PH-1@HSA** nanoparticles were successfully applied to PA imaging and PTT in nude mouse. The relatively simple molecular design of phenazine-cyanine dyes provides a new strategy for efficient photoacoustic imaging-guided photothermal therapy materials.

Experimental

Materials and measurements

Dichloromethane (DCM) was refluxed with calcium hydride and distilled before use. Ethanol (EtOH) was pre-dried over 4 Å molecular sieves before use. **PH-CHO** was synthesized according to a previous literature report.[29] All other reagents and reactants were purchased as commercial products from Energy Chemical or Sigma-Aldrich and used as received without further purification.

^{1}H NMR and ^{13}C NMR spectra were recorded on a Bruker AM 400 MHz spectrometer, and tetramethylsilane (TMS) was used as an internal standard. Electrospray ionization and time-of flight analyzer (ESI-TOF) mass spectra were determined using a Waters Micromass LCT mass spectrometer. Absorption spectra were recorded on a Varian Cary 500 UV-vis spectrophotometer. The size distribution of the nanoparticles was measured using an ALV-5000 laser light scattering spectrometer (DLS). TEM micrographs were obtained on a JEOL JSM-6360 scanning electron microscope (SEM). MTT data were measured by a microreader (Model 680, Bio-Rad).

Synthesis of PH-CHO, PH-1 and PH-2

Synthesis of 5,10-dihydrophenazine (1). Phenazine (2.94 g, 16.3 mmol) was dissolved in 70 mL ethanol and heated to 80 °C under argon atmosphere. Then, $Na_2S_2O_4$ (28.8 g, 16.5 mmol) in 250 mL ultrapure was added into the previous solution. After adding $Na_2S_2O_4$, high amount of white precipitate was observed. The mixture was heated for 1 hour and cooled to room temperature. After it was filtered, washed with water and dried *in vacuo*, a light green solid (2.81 g, 93.6%) was obtained. As it was unstable in air, compound **1** was not characterized by NMR spectra and was placed into the next reaction as soon as possible.[39]

Synthesis of 5,10-dibutylphenazine (2). 5,10-Dihydrophenazine (2.81 g, 15.3 mmol), sodium hydroxide (2.34 g, 58.6 mmol), 1 mL water and tetrabutylammonium bromide (0.4 g, 1.2 mmol) were dissolved in 25 mL DMSO. The mixture was stirred and heated to 40 °C under argon atmosphere. Then, iodobutane (4.0 mL, 35.2 mmol) was added. The mixture was stirred for another 6 hours. After cooling to room temperature, the mixture was poured into water and extracted by CH_2Cl_2. The organic phase was washed with water three times. The crude products were obtained by removing CH_2Cl_2 and purified by neutral aluminum oxide chromatography to get pure compound **2** (2.99 g, 66.0%) using petroleum ether as an eluent. ^{1}H NMR (400 MHz, C_6D_6) δ (ppm): 6.64 (m, 4H), 6.21 (m, 4H), 3.11 (m, 4H), 1.42 (m, 4H), 1.07 (m, 4H), 0.74 (*t*, *J* = 7.3 Hz, 6H). ^{13}C NMR (101 MHz, C_6D_6) δ (ppm): 137.50, 121.12, 110.96, 45.00, 26.63, 20.15, 13.77. MS (ESI, *m*/*z*): calcd for $C_{20}H_{26}N_2$: 294.21; found: 294.22.

Synthesis of PH-CHO. 5,10-Dibutylphenazine (**2**) (2.99 g, 10.1 mmol) was dissolved in 20 mL DMF and kept in an ice bath. The solution was stirred for 10 min under argon atmosphere. Then, phosphorus oxychloride (2.5 mL) was added into the flask drop by drop, and the solution was stirred for another 30 min. Subsequently, the mixture was heated for 10 hours at 60 °C. Then, the solution was poured into ice water and pH value was adjusted to weakly basic. The orange precipitate was filtered and dried. Then, pure product **PH-CHO** (0.98 g, 27.8%) was obtained by silica gel chromatography (petroleum ether/CH_2Cl_2, v : v = 2 : 1). ^{1}H NMR (400 MHz, $CDCl_3$) δ (ppm): 9.59 (s, 2H), 7.10 (dd, *J* = 8.1, 1.6 Hz, 2H), 6.72 (d, *J* = 8.2 Hz, 2H), 3.44 (m, 4H), 1.63 (m, 4H), 1.48 (m, 4H), 1.04 (*t*, *J* = 7.3 Hz, 6H). ^{13}C NMR (101 MHz, $CDCl_3$) δ (ppm): 189.89, 142.61, 135.27, 130.24, 109.85, 108.29, 45.59, 26.32, 20.13, 13.90. MS (ESI, *m*/*z*): $[M + H]^+$ calcd for $C_{22}H_{27}N_2O_2^+$: 351.2; found: 351.2.

Synthesis of PH-1. PH-CHO (160 mg, 0.45 mmol), 3*H*-indolium, 1-(2-carboxyethyl)-2,3,3-trimethyl-iodide (162 mg, 0.45 mmol), 15 mL acetonitrile and a drop of piperidine were added into a flask. The mixture was stirred and heated to 80 °C under argon atmosphere for 10 hours. Then, the solution was cooled to room temperature naturally, and acetonitrile was removed. The black-green product **PH-1** (57.1 mg, 18.6%) was obtained by silica gel chromatography (CH_2Cl_2/alcohol, v : v = 12 : 1). ^{1}H NMR (400 MHz, DMSO-d_6) δ 9.62 (s, 1H), 8.07 (d, *J* = 15.0 Hz, 1H), 7.77 (d, *J* = 6.9 Hz, 1H), 7.72 (d, *J* = 7.8 Hz, 1H), 7.54 (*t*, *J* = 7.6 Hz, 2H), 7.47 (*t*, *J* = 7.4 Hz, 1H), 7.33–7.27 (m, 2H), 6.93 (s, 1H), 6.81 (s, 1H), 6.59 (*t*, *J* = 8.7 Hz, 2H), 4.66 (*t*, *J* = 5.5 Hz, 2H), 3.67–3.61 (m, 2H), 3.60–3.55 (m, 2H), 1.71 (s, 6H), 1.52 (dd, *J* = 33.0, 11.2 Hz, 8H), 0.99 (*t*, *J* = 7.2 Hz, 6H). ^{13}C NMR (101 MHz, DMSO-d_6) δ 190.04, 189.04, 178.82, 152.37, 142.76, 141.98, 134.37, 133.36, 131.48, 129.13, 128.73, 113.95, 111.13,

109.45, 108.37, 107.37, 54.70, 50.90, 46.73, 44.18, 43.10, 33.29, 28.91, 26.17, 21.12, 19.27, 13.80, 13.65. $[M]^+$ calcd for $C_{36}H_{42}N_3O_3^+$: 564.3226; found: 564.3226.

Synthesis of PH-2. PH-CHO (124 mg, 0.35 mmol), 3*H*-indolium, 1-butyl-2,3,3-trimethyl-iodide (240 mg, 0.7 mmol), ammonium acetate (2.31 mg, 0.03 mmol) and 15 mL acetic acid were stirred in a flask under argon atmosphere. The mixture was heated to 70 °C for 8 hours and then cooled to room temperature. The solvent was removed and crude product was purified by silica gel chromatography (CH_2Cl_2/alcohol, v:v = 8:1) to obtain **PH-2** (45.3 mg, 12.9%). ^{1}H NMR (400 MHz, DMSO-d_6) δ 8.22 (d, J = 15.7 Hz, 2H), 7.87–7.81 (m, 4H), 7.69 (d, J = 8.6 Hz, 2H), 7.62–7.57 (m, 2H), 7.57–7.52 (m, 2H), 7.23 (d, J = 15.9 Hz, 2H), 7.07 (s, 2H), 6.74 (d, J = 8.9 Hz, 2H), 4.62 (*t*, J = 7.0 Hz, 4H), 3.85 (m, 2H), 3.82–3.78 (m, 2H), 1.78 (s, 12H), 1.66–1.54 (m, 8H), 1.44 (m, 8H), 1.00 (*t*, J = 7.1 Hz, 6H), 0.95 (t, J = 7.4 Hz, 6H). ^{13}C NMR (101 MHz, DMSO-d_6) δ 179.54, 171.41, 160.52, 152.34, 143.05, 142.29, 140.97, 133.36, 129.46, 128.94, 127.90, 122.94, 121.74, 117.98, 114.23, 111.92, 107.34, 105.20, 51.32, 30.09, 26.23, 22.49, 19.44, 19.28, 13.88, 13.72. MS (ESI, *m*/*z*): $[M]^{2+}$ calcd for $C_{52}H_{66}N_{42}^{2+}$: 373.2630; found: 373.2644.

Synthesis of PH-1@HSA and PH-2@HSA

Twenty mg **PH-1** was dissolved in 1 mL DMSO to obtain stock solution. Then, 27 μL solution was added into 1 mL PBS buffer containing HSA (10 mg mL^{-1}), forming nanoparticles **PH-1@HSA**. The mixture was stirred for 24 hours and subsequently centrifuged for 3 min (14 800 rpm) to remove dye unassembled with HSA. The synthesis of **PH-2@HSA** was conducted in a similar manner.

MTT assay

4T1 cells were seeded to 96 well plate (1×10^4 per well) and hatched in DEME culture medium (containing 10% fetal calf serum) for 24 hours. **PH-1@HSA** NPs were attenuated with culture medium to obtain different concentration solutions (0.7, 1.5, 3.1, 6.3, 12.5, 25, 50 and 100 μM) by replacing previous medium. 4T1 cells were placed in dark environment for 48 h. The methyl thiazolyl tetrazolium (MTT) assay was utilized to evaluate the cytotoxicity of **PH-1@HSA.** Subsequently, 4T1 cells were cultured with MTT (25 μL, 5 mg mL^{-1}) for 3 h. The absorbances at 470 nm were measured after DMSO was added (100 μL per well).

Photothermal cytotoxicity of PH-1@HSA

Photothermal cytotoxicity of **PH-1@HSA** was first measured by MTT assay. 4T1 cells were incubated with different concentration solutions (1.25, 2.5, 5, 10, 20 μM) of **PH-1@HSA** in 96 wells for 6 hours with 808 nm laser (0.8 W cm^{-2}) irradiation for 20 min, washed with fresh culture medium and incubated for another 24 hours. The subsequent process was similarity to MTT assay.

Photothermal cytotoxicity of **PH-1@HSA** was also measured by AM-PI assay *via* CLSM imaging. The experiment was divided into two groups: control group and experiment group. 4T1 cells were seeded in petri dishes at a density of 2×10^4 cells per dishes. In the experiment group, cells were treated by **PH-1@HSA** (20 μM) and exposed to 808 nm laser (0.8 W cm^{-2}) for 0, 2, 6, 10 min; in the control group, cells were exposed to 808 nm laser without NPs. Cells were further co-stained with 200 nM Calcine AM (AM) and 200 nM propidium iodide (PI). CLSM imaging was performed on Laser-scanning confocal microscopy (Leica TCS SP5).

Photothermal therapy *in vitro*

The stock solutions of **PH-1@HSA** and **PH-2@HSA** were attenuated with PBS buffer to obtain different (0, 5, 10, 20, 40, 80 μM) concentration NPs. Then, these solutions were put into tubes with laser irradiation (808 nm, 1.0 W cm^{-2}) and photographed using thermal imager per 0.5 minute to record the temperature.

Photothermal therapy *in vivo*

Fifty μL PBS solution containing 4T1 cells (5×10^6 mL^{-1}) was injected in back of nude mice, and these mice were fed till the tumors grew to ~60 mm^3. Then, these nude mice were divided into two groups (2 mice per group): control group and experimental group. In the experimental group, 200 μL **PH-1@HSA** PBS solution (500 μM) was injected in the tails of mice. After 4 h, tumors were illuminated by 808 nm laser (0.8 W cm^{-2}) and photographed by a thermal imaging camera. In the control group, pure PBS buffer was injected into mice. The nude mice were purchased from Suzhou Belda Bio-Pharmaceutical Co. Ltd, and all animal experiments were carried out according to the protocols approved by the Soochow University Laboratory Animal Center.

Conflicts of interest

There are no conflicts to declare.

Acknowledgements

This work was supported by the National Natural Science Foundation of China (21772040, 21421004, 21372082 and 21572062), the Fundamental Research Funds for the Central Universities (222201717003) and the Programme of Introducing Talents of Discipline to Universities (B16017).

Notes and references

1 A. W. Chris Twelves, M. P. Nowacki, M. Abt, H. Burris III, A. Carrato, J. Cassidy, A. Cervantes, J. Fagerberg, V. Georgoulias, F. Husseini, D. Jodrell, P. Koralewski, H. Kröning, J. Maroun, N. Marschner, J. McKendrick, M. Pawlicki, R. Rosso, J. Schüller, J. F. Seitz, B. Stabuc, J. Tujakowski, G. V. Hazel, J. Zaluski and W. Scheithauer, *N. Engl. J. Med.*, 2005, **26**, 2696–2704.
2 G. Szakacs, J. K. Paterson, J. A. Ludwig, C. Booth-Genthe and M. M. Gottesman, *Nat. Rev. Drug Discovery*, 2006, **5**, 219–234.
3 Y. S. Chen, S. J. Yoon, W. Frey, M. Dockery and S. Emelianov, *Nat. Commun.*, 2017, **8**, 15782–15792.
4 D. R. Vasilis Ntziachristos, *Chem. Rev.*, 2010, **110**, 2783–2794.
5 H. Kim, K. Chung, S. Lee, D. H. Kim and H. Lee, *Wiley Interdiscip. Rev.: Nanomed. Nanobiotechnol.*, 2016, **8**, 23–45.

6 P. Beard, *Interface Focus*, 2011, **1**, 602–631.
7 Q. Yang, J. Peng, Y. Xiao, W. Li, L. Tan, X. Xu and Z. Qian, *ACS Appl. Mater. Interfaces*, 2018, **10**, 150–164.
8 R. V. Poliraju Kalluru, C.-S. Chiang and K. C. Hwang, *Angew. Chem., Int. Ed.*, 2013, **52**, 12332–12336.
9 Y. Cai, P. Liang, Q. Tang, X. Yang, W. Si, W. Huang, Q. Zhang and X. Dong, *ACS Nano*, 2017, **11**, 1054–1063.
10 S. Wang, X. Ma, X. Hong, Y. Cheng, Y. Tian, S. Zhao, W. Liu, Y. Tang, R. Zhao, L. Song, Z. Teng and G. Lu, *ACS Nano*, 2018, **12**, 662–670.
11 P. Liu, H. Zheng, Z. Yang, L. Ba, W. Zhu, L. Lin, Y. Xiong, Z. Xu and J. Ren, *J. Mater. Chem. B*, 2018, **6**, 1688–1698.
12 Y. Zhao, W. Liu, Y. Tian, Z. Yang, X. Wang, Y. Zhang, Y. Tang, S. Zhao, C. Wang, Y. Liu, J. Sun, Z. Teng, S. Wang and G. Lu, *ACS Appl. Mater. Interfaces*, 2018, **10**, 16992–17003.
13 M. Qian, Y. Du, S. Wang, C. Li, H. Jiang, W. Shi, J. Chen, Y. Wang, E. Wagner and R. Huang, *ACS Appl. Mater. Interfaces*, 2018, **10**, 4031–4040.
14 L. Dong, G. Ji, Y. Liu, X. Xu, P. Lei, K. Du, S. Song, J. Feng and H. Zhang, *Nanoscale*, 2018, **10**, 825–831.
15 D. Cui, C. Xie, Y. Lyu, X. Zhen and K. Pu, *J. Mater. Chem. B*, 2017, **5**, 4046–4049.
16 L. Guo, G. Niu, X. Zheng, J. Ge, W. Liu, Q. Jia, P. Zhang, H. Zhang and P. Wang, *Adv. Sci.*, 2017, **4**, 1700085.
17 L. Feng, D. Tao, Z. Dong, Q. Chen, Y. Chao, Z. Liu and M. Chen, *Biomaterials*, 2017, **127**, 13–24.
18 R. J. Paproski, A. Forbrich, E. Huynh, J. Chen, J. D. Lewis, G. Zheng and R. J. Zemp, *Small*, 2016, **12**, 371–380.
19 A. Jana, K. S. Devi, T. K. Maiti and N. D. Singh, *J. Am. Chem. Soc.*, 2012, **134**, 7656–7659.
20 G.-Y. Pan, H.-R. Jia, Y.-X. Zhu, R.-H. Wang, F.-G. Wu and Z. Chen, *ACS Biomater. Sci. Eng.*, 2017, **3**, 3596–3606.
21 Y. Liu, N. Song, L. Chen, S. Liu and Z. G. Xie, *Chem. – Asian J.*, 2018, **13**, 989–995.
22 Q. Tang, W. Si, C. Huang, K. Ding, W. Huang, P. Chen, Q. Zhang and X. Dong, *J. Mater. Chem. B*, 2017, **5**, 1566–1573.
23 P. Liang, Y. Wang, P. Wang, J. Zou, H. Xu, Y. Zhang, W. Si and X. Dong, *Nanoscale*, 2017, **9**, 18890–18896.
24 X. Wu, Y. Cai, C. Wang, L. Fan, Q. Tang, X. Dong and Q. Zhang, *J. Nanosci. Nanotechnol.*, 2018, **18**, 2337–2344.
25 S. Huang, R. K. Kannadorai, Y. Chen, Q. Liu and M. Wang, *Chem. Commun.*, 2015, **51**, 4223–4226.
26 S. Huang, P. K. Upputuri, H. Liu, M. Pramanik and M. Wang, *J. Mater. Chem. B*, 2016, **4**, 1696–1703.
27 X. Li, T. Yan, H. Bin, G. Han, L. Xue, F. Liu, Y. Yi, Z.-G. Zhang, T. P. Russell and Y. Li, *J. Mater. Chem. A*, 2017, **5**, 22588–22597.
28 H. T. Turan, O. Kucur, B. Kahraman, S. Salman and V. Aviyente, *Phys. Chem. Chem. Phys.*, 2018, **20**, 3581–3591.
29 L. Yang, X. Li, Y. Qu, W. Qu, X. Zhang, Y. Hang, H. Ågren and J. Hua, *Sens. Actuators, B*, 2014, **203**, 833–847.
30 L. Yang, X. Li, J. Yang, Y. Qu and J. Hua, *ACS Appl. Mater. Interfaces*, 2013, **5**, 1317–1326.
31 X. Zhang, Y. Yan, Y. Hang, J. Wang, J. Hua and H. Tian, *Chem. Commun.*, 2017, **53**, 5760–5763.
32 L. Guo, J. Ge, W. Liu, G. Niu, Q. Jia, H. Wang and P. Wang, *Nanoscale*, 2016, **8**, 729–734.
33 M. Abbas, Q. Zou, S. Li and X. Yan, *Adv. Mater.*, 2017, **29**, 1605021.
34 Q. Chen, X. Liu, J. Zeng, Z. Cheng and Z. Liu, *Biomaterials*, 2016, **98**, 23–30.
35 Z. Li, Y. Hu, K. A. Howard, T. Jiang, X. Fan, Z. Miao, Y. Sun, F. Besenbacher and M. Yu, *ACS Nano*, 2016, **10**, 984–997.
36 R. A. Gatenby and R. J. Gillies, *Nat. Rev. Cancer*, 2004, **4**, 891–899.
37 Q. Jia, J. Ge, W. Liu, X. Zheng, M. Wang, H. Zhang and P. Wang, *ACS Appl. Mater. Interfaces*, 2017, **9**, 21124–21132.
38 P. W. B. Hildebrandt, O. Ahlers, A. Dieing, G. Sreenivasa, T. Kerner, R. Felix and H. Riess, *Critical Reviews in Oncology/Hematology*, 2002, **43**, 33–56.
39 V. R. Thalladi, T. Smolka, A. Gehrke, R. Boese and R. Sustmann, *New J. Chem.*, 2000, **24**, 143–147.

